

VIP Very Important Paper

Special Collection

www.batteries-supercaps.org

Atomically-Dispersed Fe-N₄ on 3D Hierarchical Porous Carbon for High-Performance Lithium-Sulfur Battery

Qin Bie⁺^[a], Pingbo Li⁺^[a], Hua Cheng,^[a] Sijia Zheng,^{*[a]} Jin Yu,^[a] Lei Yu,^[a] Feng Wang,^[a] Rui Wu,^[b] Jingdong Chen,^[a] and Jun Song Chen^{*[b]}

Lithium-sulfur (Li–S) battery with the advantages of high theoretical capacity and low cost is a promising technology for advanced energy storage. However, poor conductivity of the sulfur cathode, huge volume expansion, shuttling effect and sluggish catalytic conversion of lithium polysulfide hinder its commercialization. Herein, a 3D hierarchical porous carbon loaded with atomically dispersed Fe-N₄ was developed as a sulfur cathode, which not only offers enhanced electronic conductivity, but also alleviates volume expansion. Moreover,

density functional theory calculation results suggest that the Fe-N₄ sites are favorable to enhance the diffusion and promote the conversion of lithium polysulfide. Consequently, lithium-sulfur battery with 3D hierarchical porous carbon as the sulfur cathode exhibit good capacity and cycling performance, where a high initial specific capacity of 1289.3 mAh g⁻¹ can be delivered at 0.1 C, and a capacity loss of only 0.025% per cycle can be achieved for 1000 cycles at 2.0 C.

Introduction

Due to the increasing demand for new energy sources, the commonly used lithium-ion batteries (LIBs) could hardly meet the requirements because of their limited energy density (140–260 Wh kg⁻¹).^[1–3] Lithium-sulfur batteries have been considered as one of the promising candidates to replace LIBs owing to their high theoretical capacity (1675 mAh g⁻¹) and energy density (2600 Wh kg⁻¹).^[4–7] However, the poor conductivity of the cathode material S₈ would deteriorate the rate performance of the battery,^[8–10] and the shuttling of the lithium polysulfide (LiPSs) by-products during charge/discharge process causes the loss of active material and a decrease in Coulomb efficiency.^[11–14] In addition, the slow catalytic conversion of LiPSs renders them to accumulate on the surface of the cathode, further retarding the electrochemical reactions.^[10,15–17] The volume expansion of sulfur during charge-discharge process also decreases the cycling stability by inducing huge internal stress to the host material.^[18–20]

To address these problems, researchers used porous carbon as a sulfur host to improve the electrical conductivity of the

cathode.^[21–24] However, the weak interaction between the non-polar carbon and polar LiPSs cannot inhibit the shuttling effect, resulting in poor cycling performance.^[25–29] The introduction of heteroatoms (e.g., N, S, O, P, B, etc.) into the carbon-based hosts can provide powerful chemisorption for anchoring LiPSs.^[30–35] However, the slow conversion kinetics of LiPSs still leads to their accumulation on the cathode, interfering with the electrochemical processes. Recent works have shown that metal-nitrogen-carbon (M–N–C, M=Fe, Co, Ni, etc.) centers formed by transition metals on nitrogen-doped carbon can provide strong chemisorption and facilitate the conversion of LiPSs to Li₂S₂/Li₂S.^[36–42] However, the metal centers are easily aggregated during the common synthetic process, resulting in reduced number of active sites and poor catalytic activity.^[43,44]

Herein, we prepared 3D hierarchical porous carbon with abundant accessible atomically dispersed FeN₄ active sites (denoted as Fe-SA-3DHPC) as the sulfur host. The hierarchical pores of the carbon skeleton could effectively increase the sulfur loading and alleviate the volume expansion of sulfur during the charge-discharge process. Furthermore, the FeN₄ sites played dual role in the sulfur cathode: For adsorption, because of the presence of N, it would first directly interact with Li in the LiPSs and form Li–N atom pairs.^[45] More importantly, it would also induce d-orbital splitting of the coordinated Fe to interact with the 3p orbitals of the S atoms.^[45] Such a combined effect led to a strong adsorption interaction between Fe-N₄ and LiPSs. For catalytic conversion, such a Fe-N₄ site was shown to facilitate the reversible conversion between Li₂S₂ and Li₂S by lowering the diffusion energy barriers during both charge and discharge processes.^[46] As expected, the Fe-SA-3DHPC material provided a high reversible capacity of 906.4 mAh g⁻¹ after 500 cycles at a current density of 0.1 C, and a good capacity retention of 74.5% after 1000 cycles at a high current density of 2.0 C.

[a] Q. Bie,⁺ P. Li,⁺ H. Cheng, S. Zheng, J. Yu, L. Yu, F. Wang, J. Chen
Gathering and Transmission Technology Research Institute of Southwest Oil and gas field company of CNPC
Chengdu, 610000, China
E-mail: wangyizhengsijia@163.com

[b] R. Wu, Prof. J. Song Chen
School of Materials and Energy
University of Electronic Science and Technology of China
Chengdu, 611731, China
E-mail: jschen@uestc.edu.cn

[+] These authors contributed equally to this work.

Supporting information for this article is available on the WWW under
<https://doi.org/10.1002/batt.202200196>

An invited contribution to a Special Collection on IV Symposium on Advanced Energy Storage

Results and Discussion

As shown in Figure 1, the zinc and iron sources were first mixed thoroughly with mono-dispersed SiO_2 spheres (Figure 2a) in methanol, then dimethylimidazole (2-Melm) was added as the organic linker. During the formation of ZIF-8, the SiO_2 spheres were encapsulated into the ZIF-8 scaffold while the Fe ions were also incorporated (denoted as Fe-ZIF-8@ SiO_2).^[41,47,48] Subsequently, Fe-ZIF-8@ SiO_2 was pyrolyzed, in which volatilization of Zn species caused a rich micro mesoporous structure, and then the SiO_2 spheres were removed by HF etching, giving rise to a highly ordered, honey comb-like 3D porous scaffold (Figure 2b and c). Such a 3D hierarchical porous structure would facilitate the uniform dispersion of loaded sulfur and mitigate the volume expansion during long-term cycling.

Meanwhile, 3D hierarchical porous carbon without Fe atoms (denoted as 3DHPC) and 3D hierarchical porous carbon with Fe_3C nanoparticles (denoted as Fe₃C) were synthesized as control samples (Figure S1a-d). It is obvious from the transmission electron microscopy (TEM) image that Fe-SA-3DHPC has an interconnected porous structure (Figure 2d). The elemental mapping revealed that C, N, Fe, and O elements were uniformly distributed in Fe-SA-3DHPC (Figure 2e). As shown in Figure 2(f), the distribution of Fe atoms was investigated by the aberration corrected atomic-resolution high-angle annular dark-field scanning transmission electron microscopy (HAADF-STEM), and the isolated bright spots are the Fe atoms (Figure 2f, highlighted with red circles).

As shown in Figure 3(a), Fe-SA-3DHPC and 3DHPC showed one broad peak in the XRD pattern at 25°, attributing to the

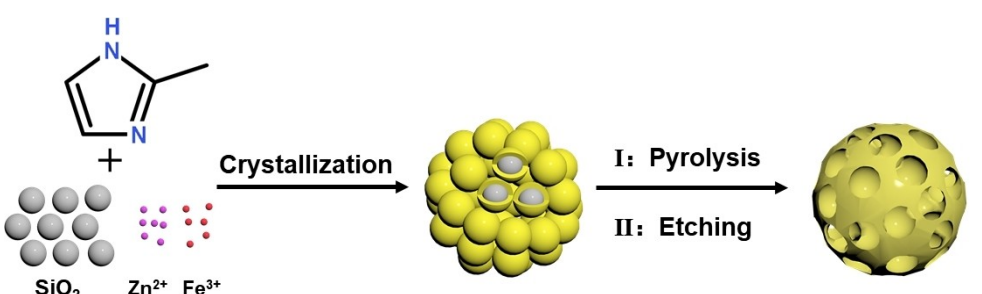


Figure 1. Schematic illustration of the synthesis process of Fe-SA-3DHPC.

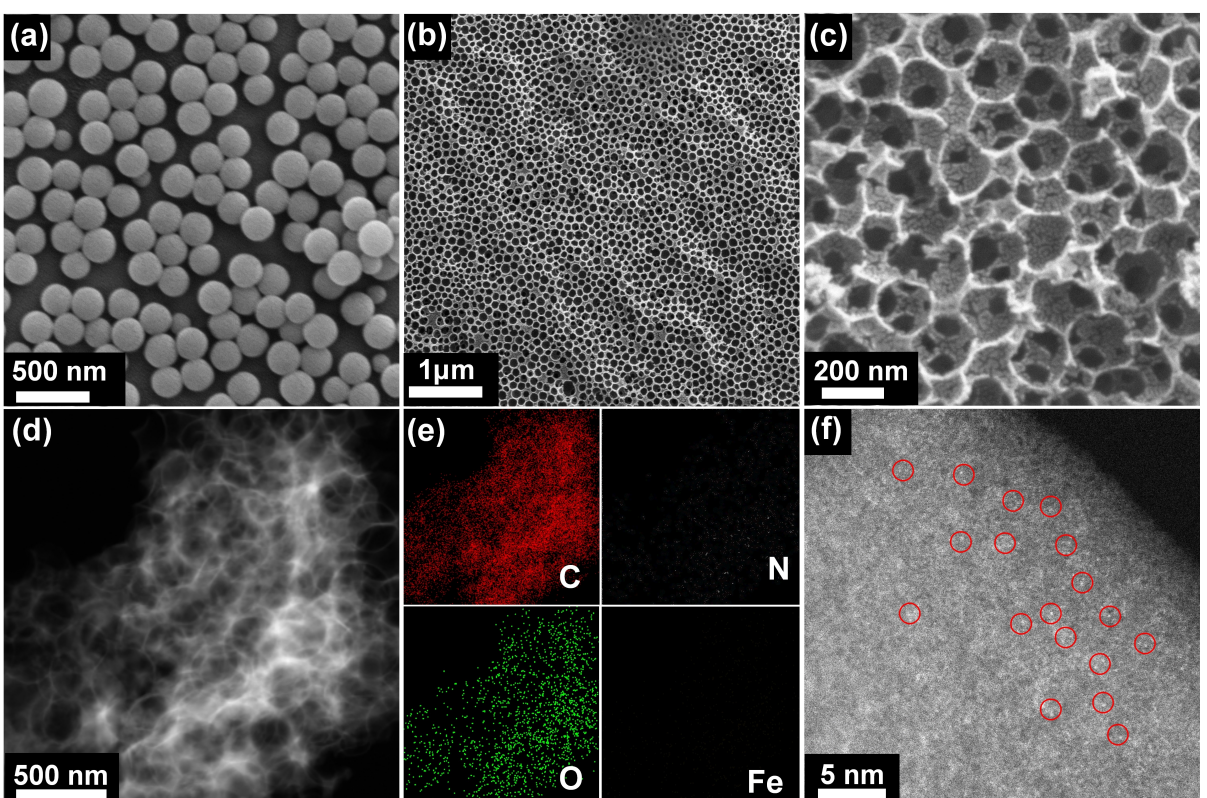


Figure 2. a) SEM image of SiO_2 nanospheres. b, c) SEM images of Fe-SA-3DHPC. d) TEM image and e) corresponding elemental mapping. f) HAADF image of Fe-SA-3DHPC.

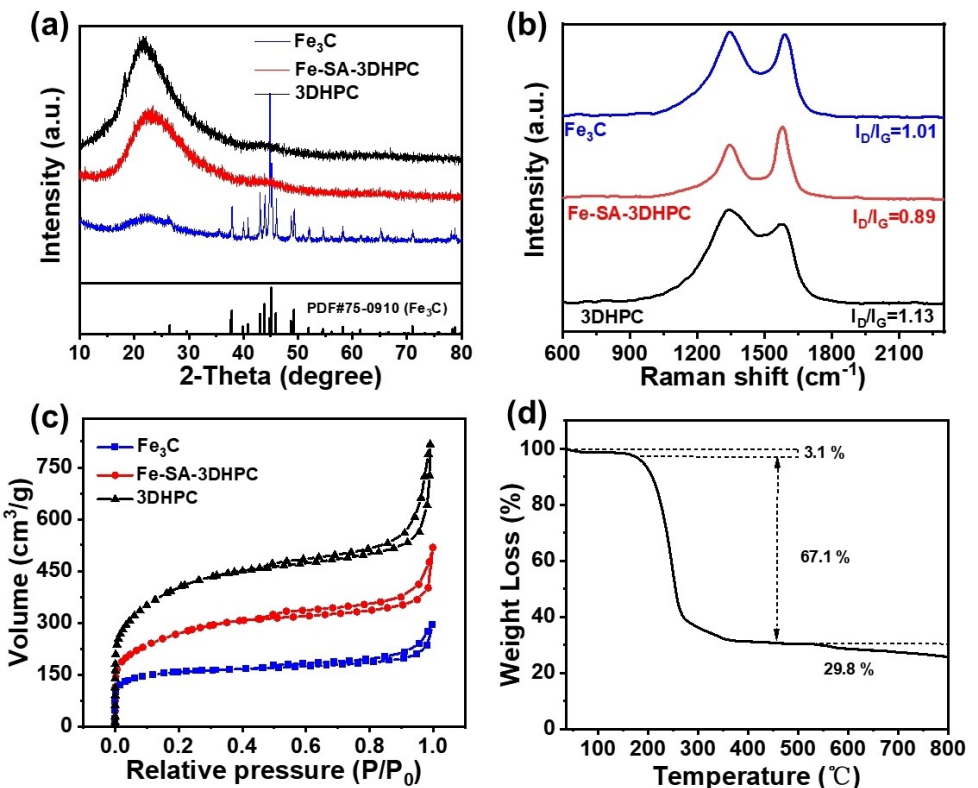


Figure 3. a) XRD patterns, b) Raman spectra, c) N₂ adsorption and desorption isotherms of 3DHPC, Fe-SA-3DHPC, Fe-NPs-3DHPC. d) TG curves of Fe-SA-3DHPC@S complex.

(002) plane of graphitized carbon. No other peaks owing to Fe species could be observed in Fe-SA-3DHPC, which is characteristic of a single atom structure. On the contrary, diffraction peaks belonging to Fe₃C (PDF#75-0910) appeared in the sample prepared with increased Fe concentration. Furthermore, disorder/graphitization degree of the obtained samples were characterized by Raman spectroscopy. The obtained samples all have two characteristic peaks at 1340 cm⁻¹ (D band) and 1580 cm⁻¹ (G band), ascribed to the lattice defects and sp²-hybridization, respectively (Figure 3b). The intensity ratio of the D and G band for Fe-SA-3DHPC, 3DHPC, Fe₃C were 0.89, 1.13, 1.01, respectively. The transition metal (i.e., Co, Ni or Fe)-catalyzed formation of graphitic carbon such as carbon nanotubes by hydrocarbon decomposition has been reported since the early 1990's,^[49] and the detailed catalytic activity of these metals during graphitization could be associated with their ability to promote the ordered rearrangement of the carbon molecules.^[50,51] Additionally, by comparing the different surface states of iron on carbon nanotubes,^[52] it has been discovered that Fe₃C demonstrated no activity.^[49,52] As a result, Fe-SA-3DHPC showed the highest graphitization level among the three samples, which could enhance the conductivity of the sulfur host and thus the rate performance.

The N₂ adsorption and desorption curves of the prepared samples showed a type-IV isotherm with a distinct hysteresis loop, indicating that the samples have microporous and mesoporous structures (Figure 3c). The corresponding Brunauer–Emmett–Teller (BET) surface areas of 3DHPC, Fe-SA-

3DHPC and Fe₃C are 1386.9, 906.4 and 515.2 m² g⁻¹, and total pore volumes are 1.264, 0.802 and 0.455 cm³ g⁻¹, respectively. Such high surface area and large pore volume could be due to the etching of SiO₂ nanospheres and evaporation of Zn-based species. Additionally, Fe-SA-3DHPC has the most abundant mesopores among the three samples (Figure S2), and the corresponding Fe-SA-3DHPC@S complex showed a sulfur content of 67.1 wt% (Figure 3d).

To further understand the surface composition and electronic state of the samples, X-ray photoelectron spectroscopy (XPS) analysis was performed. As shown in Figure 4(a), the XPS survey spectrum showed the C 1s peak at 284.8 eV, N 1s peak at ca. 400.0 eV, O 1s peak at ca. 532.0 eV and a minor Fe 2p peak at ca. 720.0 eV. The Fe signal is weak because of the low iron content in the sample,^[53] which was only 1.06 wt% as determined by inductively coupled plasma optical emission spectrometry (ICP-OES). In Figures 4(b) and S3, a distinct C–N peak could be derived from the C 1s spectra, confirming the successful N doping into the carbon skeleton.^[54–57] Figures 4(c) and S4 depicted that the N 1s high resolution spectra of Fe-SA-3DHPC could be deconvoluted into five small peaks, attributing to pyridinic-N (398.6 eV), Fe-N_x (399.8 eV), pyrrolic-N (401.1 eV), graphitic-N (402.3 eV), and oxidized-N (403.8 eV).^[53] The high-resolution XPS spectrum of Fe 2p was composed of five peaks: the peaks at 709.0 eV and 721.3 eV could be due to Fe²⁺, the ones at 711.6 eV and 724.9 eV were attributed to Fe³⁺, and the peak at 714.6 eV could be assigned to the satellite peak (Figure 4d).^[58–60]

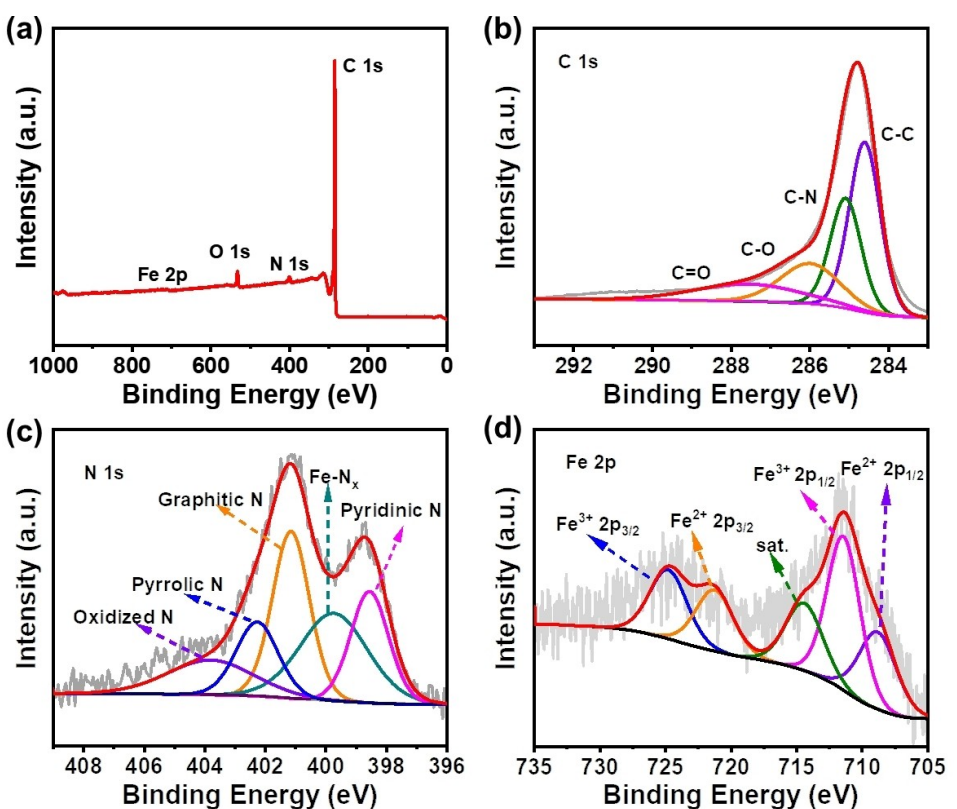


Figure 4. a) XPS spectra Survey scan of SA–Fe-3DOMC and high-resolution b) C 1s, c) N 1s and d) Fe 2p XPS spectra of SA–Fe-3DOMC.

The redox kinetics of LiPSs conversion was subsequently revealed by detailed density functional theory (DFT) calculations. Figures 5(a) and S11 illustrated the diffusion process of Li_2S on Fe-SA-3DHPC and 3DHPC at initial (IS), transition (TS) and final states (FS) with the corresponding atomic configuration and energy barrier. It is clear that the TS Li_2S on Fe-SA-3DHPC showed a much lower energy barrier of 0.036 eV than on 3DHPC (0.053 eV), suggesting a much more efficient diffusion of LiPSs on the former. Furthermore, the Gibbs free energies of the S reduction pathway of Fe-SA-3DHPC@S and 3DHPC@S cathodes were calculated (Figure 5b). Apparently, the conversion from Li_2S_2 to Li_2S exhibited

the largest increase in Gibbs free energy, suggesting that this reaction is the rate limiting step of the entire discharge process. Moreover, Fe-SA-3DHPC had a lower increase in free energy of 0.90 eV than 3DHPC (1.00 eV), indicating more favorable S reduction in the former than the latter.^[61] To investigate the effect of these samples for the adsorption of LiPSs, they were dispersed in a solution with a certain concentration of Li_2S_6 (Figure S5). It can be clearly observed from the photos that Fe-SA-3DHPC and Fe_3C possessed much stronger adsorption ability than 3DHPC after a short time of 5 min, and also after a long duration of 4 h.

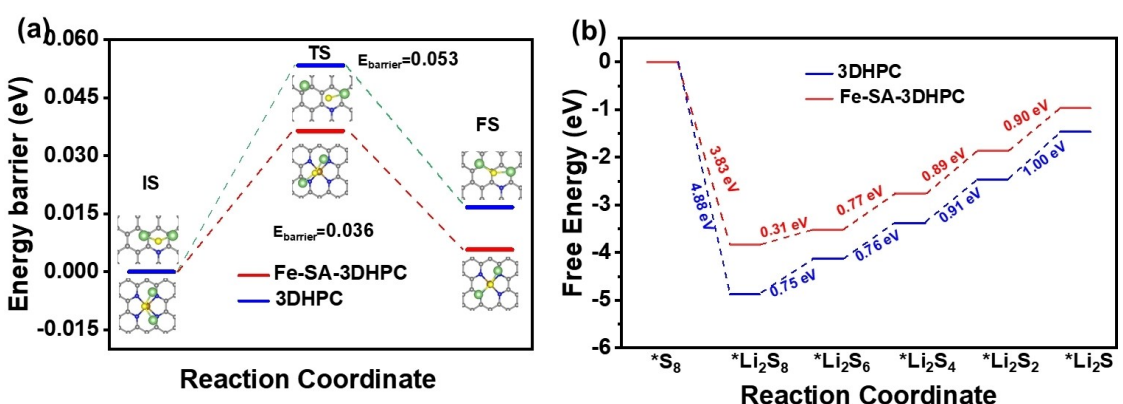


Figure 5. a) Energy barrier profiles of Li_2S cluster decomposition on Fe-SA-3DHPC and 3DHPC along with different reaction coordinates. b) Energy profiles of the reduction of Fe-SA-3DHPC and 3DHPC substrate, respectively.

The sulfur-loaded Fe-SA-3DHPC@S complex was then assembled as the cathode into a Li–S battery, and its cyclic voltammetry (CV) from 1.5 V to 3 V and constant-current discharge charging tests at different rates were conducted. It is evident from the CV curves of 3DHPC, Fe-SA-3DHPC and Fe_3C (Figures 6a and S6) that all three samples demonstrated two cathodic peaks and one anodic peak. The peaks at 2.28 V and 2.05 V could be attributed to the monomeric S_8 ring reduction to long-chain LiPSs (Li_2S_n , $4 \leq n \leq 8$) and the further conversion of LiPSs to insoluble $\text{Li}_2\text{S}_2/\text{Li}_2\text{S}$, respectively. While the anodic peak appearing at 2.52 V could be due to the oxidation of insoluble short-chain $\text{Li}_2\text{S}_2/\text{Li}_2\text{S}$ to soluble long-chain LiPSs and eventually to S_8 .

The galvanostatic charge/discharge tests of the samples were conducted between 0.1 and 5 C (Figures 6b and S7). The discharge curves exhibited two significant voltage plateaus at 2.3 V and 2.1 V, attributing to the formation of long-chain LiPSs (Li_2S_n , $4 \leq n \leq 8$) and short-chain LiPSs ($\text{Li}_2\text{S}_2/\text{Li}_2\text{S}$), respectively.^[31] The curves maintained similar pattern even at the highest current of 5.0 C, indicating efficient kinetic process even at high rates. Figure 6c compares the rate performance of

these samples. The Fe-SA-3DHPC cathode demonstrated the highest specific capacity at all rates. As the current increased to 5.0 C, Fe-SA-3DHPC delivered the highest specific capacity of 680.8 mAh g⁻¹, significantly higher than those of Fe_3C (490.2 mAh g⁻¹) and 3DHPC (311.9 mAh g⁻¹). When the current rate was reduced to 0.1 C, the capacity of Fe-SA-3DHPC could be almost restored to the original value, indicating its excellent electrochemical reversibility. The charge transfer resistance of these cathodes were investigated via electrochemical impedance spectroscopy (EIS) analysis. As shown in Figure S8, the Fe-SA-3DHPC cathode shows the semicircle with the smallest diameter, suggesting its lowest charge transfer resistance, which could be attributed to the promoted redox and conversion of LiPSs.^[62]

CV tests were performed at different scan rates from 0.1 to 0.6 mVs⁻¹ to further unravel the electrochemical kinetic processes of the 3DHPC, Fe-SA-3DHPC and Fe_3C cathode (Figure S9a–c). As shown in Figure S9(d and e), it is obvious that the calculated *b* values of Fe-SA-3DHPC are higher than those of 3DHPC and Fe_3C , implying that Fe-SA-3DHPC with Fe single atom active sites can effectively catalyze the conversion of LiPSs,^[63] and also accelerate

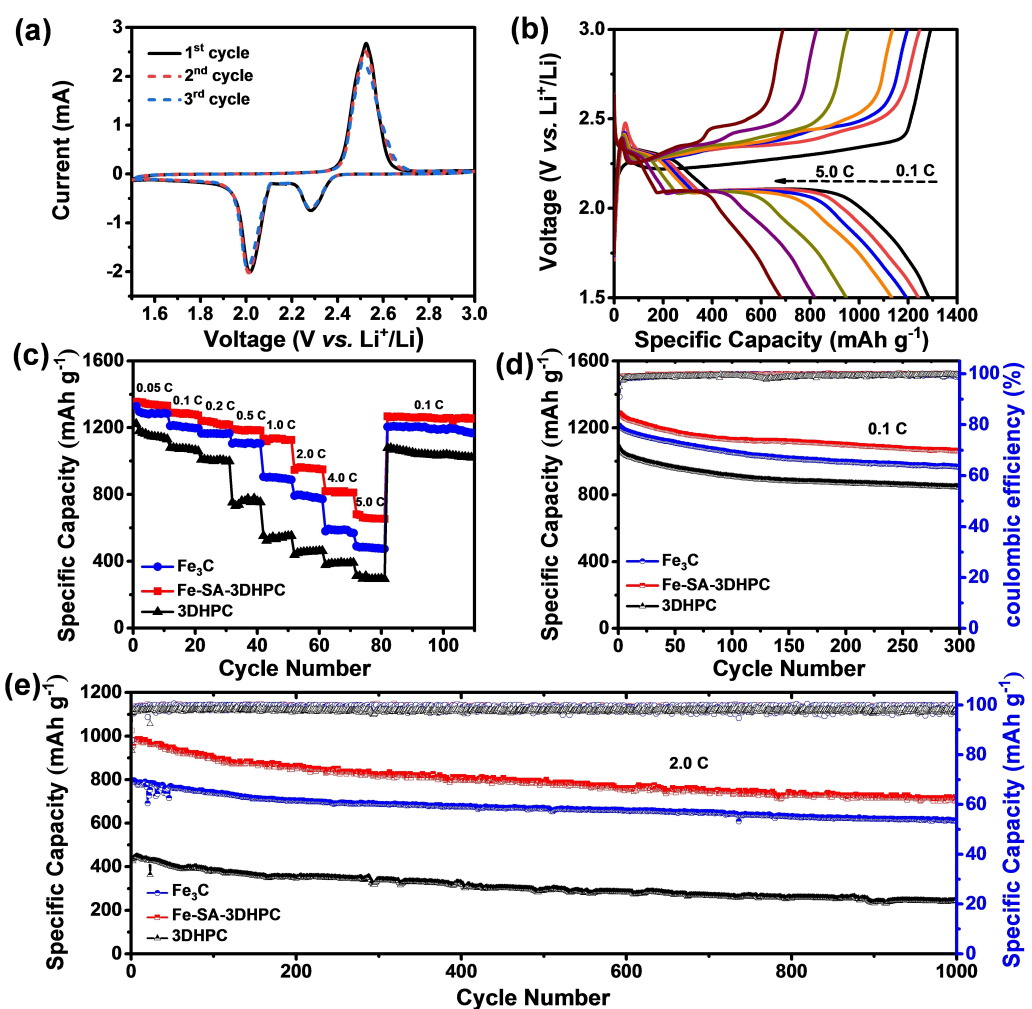


Figure 6. a) CV curves of Fe-SA-3DHPC. b) Galvanostatic charge and discharge profiles of Fe-SA-3DHPC. c) Rate capabilities of 3DHPC, Fe-SA-3DHPC and Fe_3C . d) The cycling performance at 0.1 C. e) the long-term cycling performance at 2.0 C.

the transfer of Li^+ (Figure S9).^[64] As for the cycling stability shown in Figure 6d, the Fe-SA-3DHPC cathode showed a high initial specific capacity of $1289.3 \text{ mAh g}^{-1}$ at a current density of 0.1 C, and dropped to $1064.3 \text{ mAh g}^{-1}$ after 300 cycles, corresponding to a capacity retention of about 82.55%. As a comparison, the specific capacities of 3DHPC and Fe_3C cathodes exhibited much poorer cycling stability than Fe-SA-3DHPC with specific capacities of 966.7 and 845.6 mAh g^{-1} after 300 cycles, respectively. The long-term cycling performance of the three samples was also measured at higher current densities of 2.0 C and 5.0 C (Figures 6e and S11). The Fe-SA-3DHPC cathode delivered an initial specific capacity of 948.6 mAh g^{-1} at 2.0 C and 706.6 mAh g^{-1} after 1000 cycles with a capacity loss rate of 0.025% per cycle. In contrast, the initial capacities of 3DHPC and Fe_3C cathodes were only 794.6 and 436.8 mAh g^{-1} . After 1000 cycles, the specific capacity dropped 610.6 and 243.5 mAh g^{-1} . Even at a current density of 5.0 C, Fe-SA-3DHPC could reach a specific capacity of 516.8 mAh g^{-1} after 1000 cycles, much higher than that of 3DHPC (103.2 mAh g^{-1}) and Fe_3C (357.9 mAh g^{-1}).

Conclusion

In summary, 3D hierarchical porous carbon with Fe single atom active sites were synthesized as an efficient sulfur host. Experimental results comprehensively demonstrated that the Fe single atom active center not only provided strong chemisorption capacity but also catalyzed the conversion of LiPSs. At the meantime, this special 3D hierarchical porous structure could effectively alleviate the volume expansion during charge/discharge. DFT calculation results revealed that the presence of $\text{Fe}-\text{N}_4$ s sites would effectively enhance the diffusion and also facilitate the catalytic conversion of the LiPSs intermediates. As a result, the Fe-SA-3DHPC cathode delivered a high specific capacity of 948.6 mAh g^{-1} at 2.0 C over 1000 cycles with a capacity decay rate of 0.025% per cycle. This category of 3D hierarchical porous carbons decorated with atomic dispersed catalytic sites exhibited great potential for Li–S battery with higher energy density and long cycle life.

Experimental Section

Materials

$\text{Zn}(\text{NO}_3)_2 \cdot 6\text{H}_2\text{O}$ (98%, Sinopharm Chem. reagent Co., Ltd, China), $\text{FeCl}_3 \cdot 6\text{H}_2\text{O}$ (98%, Sinopharm Chem. reagent Co., Ltd, China), methanol (99.5%, Aldrich Industrial Co.), ammonia solution (28~30%, Sinopharm Chem. reagent Co., Ltd, China), 2-methylimidazole (98%, Aldrich Industrial Co.), Tetraethyl orthosilicate (25%, Sigma Aldrich). All used chemical reagents are analytical grade without further purification.

Synthesis of silica nanosphere

Silica nanospheres employed as templates were synthesized by a modified Stöber method.^[65] Typically, tetraethyl orthosilicate (15 mL) was dropwise added to a mixture of ammonia solution (28~30%, 5 mL), ethanol (225 mL) and deionized water (30 mL).

After 2 h of continuous stirring, silica spheres were obtained by centrifugation, washing and vacuum drying overnight.

Synthesis of Fe-SA-3DHPC

First, silica nanospheres (0.5 g), $\text{Zn}(\text{NO}_3)_2 \cdot 6\text{H}_2\text{O}$ (0.87 g) and $\text{FeCl}_3 \cdot 6\text{H}_2\text{O}$ (25 mg) were added to 20 mL of methanol solution. Meanwhile, 2-methylimidazole (0.98 g) was added to 20 mL of methanol in another beaker. Subsequently, the two solutions were mixed and stirred thoroughly for 2 h. Next, the two above solutions were rapidly mixed together and heated at 60 °C for 24 h. The obtained $\text{SiO}_2@\text{ZIF-8-Fe}$ nanocomposites were pyrolyzed at 900 °C for 2 h under Ar atmosphere with a ramp of 2 °C min⁻¹. Finally, the Fe-SA-3DHPC catalyst was obtained by HF leaching (8%, 40 mL) for 12 h and a second heat-treatment in Ar for 1 h at 900 °C. For comparison, the contrast samples were prepared under conditions similar to that used for Fe-SA-3DHPC. 3DHPC was synthesized without ferric chloride, and Fe_3C was synthesized with 100 mg ferric chloride by the same method.

Preparation of free-standing Fe-SA-3DHPC-S composite

Briefly, sublimated sulfur (140 mg) and Fe-SA-3DHPC (60 mg) were well-mixed in a ratio of 7:3. The as-prepared mixture was transferred into a Teflon-lined autoclave and then heated at 155 °C for 12 h under an Ar atmosphere. For comparison purposes, Fe-SA-3DHPC and Fe_3C composites were also prepared under the same experimental conditions.

Electrochemical measurements

Briefly, Fe-SA-3DHPC@S was well-mixed with conductive carbon black (Super-P) and Polyvinylidene Fluoride (PVDF) in N-methyl-2-pyrrolidone (NMP) solvent at a weight ratio of 8:1:1. Then the mixture was directly coated onto a cleaned aluminum foil and dried at 60 °C overnight in a vacuum oven to remove the NMP. Coin batteries (CR2025) with an Fe-SA-3DHPC@S cathode, Celgard 2400 porous separators, and Li-foil anode were assembled in an argon-filled glovebox, and the mass loading of active sulfur for working electrode is controlled in the range of 2.0~2.2 mg cm⁻². The electrolyte used in this test was 1.0 M bis(trifluoromethane)sulfonimide lithium (LiTFSI) dissolved in a mixed solvent of 1,3-dioxolane (DOL) and 1,2-dimethoxyethane (DME) (1:1 by volume). The addition of approximately 40 μL of electrolyte in each cell. The cyclic voltammograms (CV) curves were carried out on a BioLogic Science Instruments VMP3 electrochemical workstation at different scan rates from 0.10 to 0.60 mV s⁻¹ with a voltage window of 1.5~3.0 V. Electrochemical impedance spectroscopy (EIS) were also performed on the same electrochemical workstation in the frequency range from 100 kHz to 0.1 Hz with an amplitude of 5 mV.

Acknowledgements

The authors thank the National Key R&D Program of China for the financial support through 2021YFB2401900.

Conflict of Interest

The authors declare no conflict of interest.

Data Availability Statement

The data that support the findings of this study are available from the corresponding author upon reasonable request.

Keywords: lithium-sulfur batteries • Fe-N₄ single atom • hierarchical porous carbon • conversion kinetics • facilitated diffusion

- [1] N. Liu, Z. Lu, J. Zhao, M. T. McDowell, H. W. Lee, Zhao, W. Y. Cui, *Nat. Nanotechnol.* **2014**, *9*, 187–192.
- [2] P. G. Bruce, S. A. Freunberger, Hardwick, L. J. J. M. Tarascon, *Nat. Mater.* **2011**, *11*, 19–29.
- [3] Q. Pang, X. Liang, Kwok, C. Y. L. F. Nazar, *Nat. Energy* **2016**, *1*, 16132.
- [4] Z. Du, X. Chen, W. Hu, C. Chuang, S. Xie, A. Hu, W. Yan, X. Kong, X. Wu, Ji, H. L. J. Wan, *J. Am. Chem. Soc.* **2019**, *141*, 3977–3985.
- [5] Y. Son, J. S. Lee, Y. Son, Jang, J. H. J. Cho, *Adv. Energy Mater.* **2015**, *5*, 1500110.
- [6] Y. X. Yin, S. Xin, Guo, Y. G. L. J. Wan, *Angew. Chem. Int. Ed. Engl.* **2013**, *52*, 13186–13200.
- [7] N. Angulakshmi, R. B. Dhanalakshmi, S. Sathya, Ahn, J. H. A. M. Stephan, *Batteries & Supercaps* **2021**, *4*, 1064–1095.
- [8] X. Tao, J. Wang, C. Liu, H. Wang, H. Yao, G. Zheng, Z. W. Seh, Q. Cai, W. Li, G. Zhou, Zu, C. Y. Cui, *Nat. Commun.* **2016**, *7*, 11203.
- [9] T. Wang, J. Zhu, Z. Wei, H. Yang, Z. Ma, R. Ma, J. Zhou, Y. Yang, L. Peng, H. Fei, Lu, B. X. Duan, *Nano Lett.* **2019**, *19*, 4384–4390.
- [10] S. Jiang, S. Huang, M. Yao, J. Zhu, Liu, L. Z. Niu, *Chin. Chem. Lett.* **2020**, *31*, 2347–2352.
- [11] M. Zhao, H. J. Peng, Z. W. Zhang, B. Q. Li, X. Chen, J. Xie, X. Chen, J. Y. Wei, Zhang, Q. J. Q. Huang, *Angew. Chem. Int. Ed. Engl.* **2019**, *58*, 3779–3783.
- [12] Z. Liu, L. Zhou, Q. Ge, R. Chen, M. Ni, W. Utetiwabo, Zhang, X. W. Yang, *ACS Appl. Mater. Interfaces* **2018**, *10*, 19311–19317.
- [13] L. Ma, W. Zhang, L. Wang, Y. Hu, G. Zhu, Y. Wang, R. Chen, T. Chen, Z. Tie, Liu, J. Z. Jin, *ACS Nano* **2018**, *12*, 4868–4876.
- [14] Z. Bian, Y. Xu, T. Yuan, C. Peng, Y. Pang, Yang, J. S. Zheng, *Batteries & Supercaps* **2019**, *2*, 560–567.
- [15] G. Hu, Z. Sun, C. Shi, R. Fang, J. Chen, P. Hou, C. Liu, Cheng, H. M. F. Li, *Adv. Mater.* **2017**, *29*, 1603835.
- [16] M. Gao, W.-Y. Zhou, Y.-X. Mo, T. Sheng, Y. Deng, L. Chen, K. Wang, Tan, Y. H. Zhou, *Adv. Powder Metall. Part. Mater.* **2021**.
- [17] C. Geng, W. Hua, D. Wang, G. Ling, Zhang, C. Q. H. Yang, *SusMat* **2021**, *1*, 51–65.
- [18] Z. Li, J. T. Zhang, Y. M. Chen, Li, J. X. W. Lou, *Nat. Commun.* **2015**, *6*, 8850.
- [19] C. G. Wang, H. W. Song, C. C. Yu, Z. Ullah, Z. X. Guan, R. R. Chu, Y. F. Zhang, L. Y. Zhao, Li, Q. L. W. Liu, *J. Mater. Chem. A* **2020**, *8*, 3421–3430.
- [20] S. J. Fretz, M. Agostini, P. Jankowski, P. Johansson, Matic, A. A. E. C. Palmqvist, *Batteries & Supercaps* **2020**, *3*, 757–765.
- [21] Z. Yu, M. Liu, D. Guo, J. Wang, X. Chen, J. Li, H. Jin, Z. Yang, Chen, X. S. Wang, *Angew. Chem. Int. Ed. Engl.* **2020**, *59*, 6406–6411.
- [22] Y. Du, R. Huang, X. Lin, S. Khan, Zheng, B. R. Fu, *Langmuir* **2020**, *36*, 14507–14513.
- [23] S. Zeng, X. Li, H. Zhong, Chen, S. Y. Mai, *Small Methods* **2019**, *3*, 1900028.
- [24] Y. Gong, C. Fu, A. Dong, H. Zhou, Li, H. Y. Kuang, *Batteries & Supercaps* **2018**, *1*, 192–201.
- [25] Y. Qiu, L. Fan, M. Wang, X. Yin, X. Wu, X. Sun, D. Tian, B. Guan, Tang, D. N. Zhang, *ACS Nano* **2020**, *14*, 16105–16113.
- [26] H. Geng, Y. Peng, L. Qu, Zhang, H. M. Wu, *Adv. Energy Mater.* **2020**, *10*, 1903030.
- [27] D. Su, Cortie, M. G. Wang, *Adv. Energy Mater.* **2017**, *7*, 1602014.
- [28] B. Krüner, T. S. Dörr, H. Shim, J. Sann, Janek, J. V. Presser, *Batteries & Supercaps* **2018**, *1*, 83–94.
- [29] M. Yu, S. Zhou, Z. Wang, Y. Wang, N. Zhang, S. Wang, Zhao, J. J. Qiu, *Energy Storage Mater.* **2019**, *20*, 98–107.
- [30] Y. N. Liu, Z. Y. Wei, B. Zhong, H. T. Wang, L. Xia, T. Zhang, X. M. Duan, D. C. Jia, Zhou, Y. X. X. Huang, *Energy Storage Mater.* **2021**, *35*, 12–18.
- [31] L. Ma, R. Chen, G. Zhu, Y. Hu, Y. Wang, T. Chen, Liu, J. Z. Jin, *ACS Nano* **2017**, *11*, 7274–7283.
- [32] Y. L. Ding, P. Kopold, K. Hahn, P. A. van Aken, Maier, J. Y. Yu, *Adv. Funct. Mater.* **2016**, *26*, 1112–1119.
- [33] J. Song, M. L. Gordin, T. Xu, S. Chen, Z. Yu, H. Sohn, J. Lu, Y. Ren, Duan, Y. D. Wang, *Angew. Chem. Int. Ed. Engl.* **2015**, *54*, 4325–4329.
- [34] J. X. Song, T. Xu, M. L. Gordin, P. Y. Zhu, D. P. Lv, Y. B. Jiang, Y. S. Chen, Duan, Y. H. D. H. Wang, *Adv. Funct. Mater.* **2014**, *24*, 1243–1250.
- [35] Y. Liu, H. Guo, B. Zhang, G. Wen, R. Vajtai, L. Wu, Ajayan, P. M. L. Wang, *Batteries & Supercaps* **2020**, *3*, 1201–1208.
- [36] H. Shi, X. Ren, J. Lu, C. Dong, J. Liu, Q. Yang, Chen, J. Z. S. Wu, *Adv. Energy Mater.* **2020**, *10*, 2002271.
- [37] C. Lu, Y. Chen, Yang, Y. X. Chen, *Nano Lett.* **2020**, *20*, 5522–5530.
- [38] S. Zhang, X. Ao, J. Huang, B. Wei, Y. Zhai, D. Zhai, W. Deng, C. Su, Wang, D. Y. Li, *Nano Lett.* **2021**, *21*, 9691–9698.
- [39] Y. J. Chen, S. F. Ji, C. Chen, Q. Peng, Wang, D. S. Y. D. Li, *Joule* **2018**, *2*, 1242–1264.
- [40] M. Yu, S. Zhou, Z. Wang, W. Pei, X. Liu, C. Liu, C. Yan, X. Meng, S. Wang, Zhao, J. J. Qiu, *Adv. Funct. Mater.* **2019**, *29*.
- [41] X. Wan, X. Liu, Y. Li, R. Yu, L. Zheng, W. Yan, H. Wang, Xu, M. J. Shui, *Nat. Catal.* **2019**, *2*, 259–268.
- [42] M. Qiao, Y. Wang, Q. Wang, G. Hu, X. Mamat, Zhang, S. S. Wang, *Angew. Chem. Int. Ed.* **2020**, *59*, 2688–2694; *Angew. Chem.* **2020**, *132*, 2710–2716.
- [43] H. Zhang, Y. Lu, W. Han, J. Zhu, Zhang, Y. W. Huang, *Chem. Eng. J.* **2020**, *393*.
- [44] F. Xu, Y. Zhou, X. Zhai, H. Zhang, H. Liu, E. H. Ang, Y. Lu, Z. Nie, Zhou, M. J. Zhu, *Small Methods* **2022**, *6*, 2101212.
- [45] X. Han, Zhang, Z. X. Xu, *J. Mater. Chem. A* **2021**, *9*, 12225–12235.
- [46] Z. Du, X. Chen, W. Hu, C. Chuang, S. Xie, A. Hu, W. Yan, X. Kong, X. Wu, Ji, H. L.-J. Wan, *J. Am. Chem. Soc.* **2019**, *141*, 3977–3985.
- [47] Z. Zhu, H. Yin, Y. Wang, C. H. Chuang, L. Xing, M. Dong, Y. R. Lu, G. Casillas-Garcia, Y. Zheng, S. Chen, Y. Dou, P. Liu, Cheng, Q. H. Zhao, *Adv. Mater.* **2020**, *32*, 2004670.
- [48] M. Qiao, Y. Wang, Q. Wang, G. Hu, X. Mamat, Zhang, S. S. Wang, *Angew. Chem. Int. Ed. Engl.* **2020**, *59*, 2688–2694.
- [49] D. S. Bethune, C. H. Kiang, M. S. de Vries, G. Gorman, R. Savoy, Vazquez, J. R. Beyers, *Nature* **1993**, *363*, 605–607.
- [50] A. Moisala, Nasibulin, A. G. E. I. Kauppinen, *J. Phys. Condens. Matter* **2003**, *15*, S3011–S3035.
- [51] Jourdain, V. C. Bichara, *Carbon* **2013**, *58*, 2–39.
- [52] R. T. K. Baker, J. R. Alonzo, Dumesic, J. A. D. J. C. Yates, *J. Catal.* **1982**, *77*, 74–84.
- [53] F. Pan, B. Li, E. Sarnello, Y. Fei, X. Feng, Y. Gang, X. Xiang, L. Fang, T. Li, Y. H. Hu, Wang, G. Y. Li, *ACS Catal.* **2020**, *10*, 10803–10811.
- [54] J. J. Cai, Q. Y. Zhou, B. Liu, X. F. Gong, Y. L. Zhang, K. Goh, D. M. Gu, L. Zhao, Sui, X. L. Z. B. Wang, *Nanoscale* **2020**, *12*, 973–982.
- [55] C. Guo, Y. Li, W. Liao, Y. Liu, Z. Li, L. Sun, C. Chen, J. Zhang, Si, Y. L. Li, *J. Mater. Chem. A* **2018**, *6*, 13050–13061.
- [56] Y. Lu, H. Zhang, H. Liu, Z. Nie, F. Xu, Y. Zhao, Zhu, J. W. Huang, *Nano Lett.* **2021**, *21*, 9651–9660.
- [57] Y. Ding, Q. Zhang, K. Rui, F. Xu, H. Lin, Y. Yan, H. Li, Zhu, J. W. Huang, *Nano Lett.* **2020**, *20*, 8818–8824.
- [58] G. Gan, X. Li, L. Wang, S. Fan, J. Mu, Wang, P. G. Chen, *ACS Nano* **2020**, *14*, 9929–9937.
- [59] Z. Y. Wu, X. X. Xu, B. C. Hu, H. W. Liang, Y. Lin, Chen, L. F. S. H. Yu, *Angew. Chem. Int. Ed. Engl.* **2015**, *54*, 8179–8183.
- [60] Z. Zhang, M. Dou, H. Liu, Dai, L. F. Wang, *Small* **2016**, *12*, 4193–4199.
- [61] C. Ma, Y. Zhang, Y. Feng, N. Wang, L. Zhou, C. Liang, L. Chen, Y. Lai, X. Ji, Yan, C. W. Wei, *Adv. Mater.* **2021**, *33*, 2100171.
- [62] Y. Zhong, L. Yin, P. He, W. Liu, Wu, Z. H. Wang, *J. Am. Chem. Soc.* **2018**, *140*, 1455–1459.
- [63] J. T. Liu, S. H. Xiao, X. Q. Liu, R. Wu, X. B. Niu, Y. Xiang, Chen, J. S. C. H. Yang, *Chem. Eng. J.* **2021**, *423*, 130246.
- [64] J. T. Liu, S. H. Xiao, L. Chang, L. Lai, R. Wu, Y. Xiang, Liu, X. Q. J. S. Chen, *J. Energy Chem.* **2021**, *56*, 343–352.
- [65] A. I. Douka, Y. Xu, H. Yang, S. Zaman, Y. Yan, H. Liu, Salam, M. A. B. Y. Xia, *Adv. Mater.* **2020**, *32*, 2002170.

Manuscript received: April 26, 2022

Revised manuscript received: May 26, 2022

Accepted manuscript online: May 31, 2022

Version of record online: June 15, 2022